Electrical Power and Energy Systems 177 (2026) 111797

Contents lists available at ScienceDirect

International Journal of Electrical Power and Energy Systems

journal homepage: www.elsevier.com/locate/ijepes

Improvements of a multi-agent secondary controller for reconnecting a microgrid to the main grid

Andrés Tomás-Martín [a,*], Javier Roldán-Pérez [b], Njegos Jankovic [b], Sauro Yagüe [c], Lukas Sigrist [a], Aurelio García-Cerrada [d]

[a] IIT, ICAI Engineering School, Comillas Pontifical University, Alberto Aguilera, 23, 28015, Madrid, Spain
[b] Electrical Systems Unit, IMDEA Energy, Móstoles, Spain
[c] Industrial Engineering Department, IQS, Ramón Llull Univesity, Barcelona, Spain
[d] IIT & Department of Electronics, Control and Communications, ICAI Engineering School, Comillas Pontifical University, Alberto Aguilera, 23, 28015, Madrid, Spain

ARTICLE INFO

Keywords:
Microgrid
Synchronisation
Decentralised control
Multi-agent systems
Small-signal stability

ABSTRACT

Microgrids (MGs) can work either connected to or disconnected from the main grid, and seamless transition between modes is essential for reliable operation. Even though centralised secondary controllers are the obvious choice to resynchronise MGs with the main grid, and to control their power exchange, decentralised multi-agent secondary controllers have been proposed recently because they simplify the communication system required. However, aspects such as communication delays and implementation details have not received enough attention. This paper describes an improved decentralised multi-agent secondary controller based on consensus to resynchronise a MG with the main grid and control the power exchange afterwards. The effects of communication delays between agents and the potentially dangerous active power transients required to synchronise the MG were studied by small signal stability analysis and numerical simulations. The paper shows that both problems can be addressed with a systematic design of the decentralised secondary controller combined with derivative droop primary controllers. Results were validated in a real MG consisting of four 15 kVA power converters, electrical lines and loads, a 75 kVA grid emulator, and an industrial communication infrastructure. The proposed algorithm has been validated in a large system consisting of 69 buses, which includes seven grid-forming converters and primarily resistive lines. Additionally, the algorithm has been tested in scenarios with limited available energy from the converters and taking into account the control of the voltage amplitude difference between the microgrid and the main grid.

1. Introduction

Microgrids (MGs) are an effective solution to facilitate the integration of renewable energy sources (RESs) and distributed generators (DGs) in electrical networks. A MG is a small-scale power system that can operate connected to the main grid or as an island [1]. The transition between these two modes is essential and must be carried out seamlessly with accurate synchronisation and avoiding undesired transients [2].

A DG placed at the point of common coupling between the microgrid and the main grid (PCC) can be used to control voltage and frequency at that point to synchronise the MG [3]. However, this solution is not always practical, and alternatives have been sought in the literature for some time. For example in [4], the angle difference between the grid and the MG at the PCC is forced to be zero before reconnection using a central proportional-integral (PI) controller that calculates the frequency set point for all Grid-forming VSCs (GFo-VSCs) in the microgrid. A centralised control approach is the most common alternative so far [5]. However, with the current development of DGs and smart grids, conventional centralised controllers may be replaced by multi-agent decentralised controllers, which can simplify the communication infrastructure. One of the most common techniques for decentralised control is consensus-based control [6], where each independent agent acts based on the information received from a limited number of *neighbours*. Consensus algorithms have recently gained attention for applications in AC and DC MGs [7,8].

A consensus-based cooperative synchronisation between a microgrid and the main grid was proposed by Sun et al. [9]. In [10], this idea was further improved by means of an additional low-pass filter

* Corresponding author.
E-mail address: atomas@comillas.edu (A. Tomás-Martín).

https://doi.org/10.1016/j.ijepes.2026.111797
Received 12 May 2025; Received in revised form 20 February 2026; Accepted 19 March 2026
Available online 25 March 2026

(LPF) that smooths the synchronisation transient. A similar approach is presented by Li et al. [11], but, in this case, using sliding mode voltage and current controllers. Recently, in a previous work of the authors of this manuscript, a method based on a saturator was proposed [12]. With this method, synchronisation speed is limited to prevent unwanted power oscillations in the MG. A decentralised algorithm to synchronise MGs based on droop-controlled DGs is presented by Khan et al. [13], in which one DG is in charge of the synchronisation. Even though these works already presented the main ideas to resynchronise MGs, none of these references considers implementation aspects nor the effect of delays in the communication between DGs. However, communication delays between agents affect the stability of multi-agent algorithms, as shown in [14]. The authors of that reference calculate the maximum delay compatible with a stable secondary controller. This limit depends on the properties of the communication graph between agents and has already been explored in [15], although the analysis neglected the effect of the controllers of the DGs. In this regard, Coelho et al. [16] proposed an extension of the small-signal model of a MG with a multi-agent secondary control that includes constant communication time delays. It was found that, by increasing the time delay, some specific system eigenvalues approach the imaginary axis. A similar eigenvalue analysis was conducted by Chen et al. [17] to determine the stability boundaries of a consensus-based secondary control in the presence of communication delays, for a DC MGs.

The effect of communication delays in the MG stability has been analysed for an adaptative triggered consensus algorithm [18]. However, none of these works was focused on synchronisation controllers, which have specific problems such as active power transients. Moreover, in these works, the power flow between DGs is always addressed from the secondary controller point of view, overlooking the capacity of primary controllers to limit active-power transients.

Shahab et al. [19] highlight the importance of sensor noise in consensus algorithms, in addition to communication delays. This study was later expanded to consider the effect of additive Gaussian noise and time-varying stochastic delays [20]. In that work, it was shown that DGs may receive incomplete or imprecise information from neighbours due to the fading caused by multi-path propagation. However, these issues are out of the scope of this work since a reliable protocol (TCP/IP) among agents is used and adequate data integrity is guaranteed.

In this paper, a multi-agent secondary controller for resynchronising MGs formed by GFo-VSCs with the main grid is proposed, analysed and then implemented and validated in a laboratory. The proposed controller is also capable of imposing the required active-power exchange between the microgrid and the main grid, once the resynchronisation takes place. This paper focuses on the implementation aspects of this controller, which were not addressed in previous references. More precisely, the effect of communication delays is modelled and explored, together with the active-power flow between DGs during the synchronisation process. A detailed small-signal analysis is used to assess the impact of communication delays, while active-power transients are studied by using a simplified model of the power flow. These tools are subsequently used to design a synchronisation controller that guarantees the stability of the MG and limits the active-power flow during the synchronisation process. This paper demonstrates that active-power flows can be greatly reduced by using a derivative droop controller. In fact, a conventional but carefully designed PI controller, together with the derivative droop, is enough to satisfy all the requirements.

The main features of the proposed controller are validated by simulations in MATLAB/Simulink [21], and in a laboratory consisting of four 15 kVA power converters (acting as DGs). The main contribution of this paper compared to the state-of-the-art work is highlighted in Table 1. The main contribution of this proposed algorithm is its ability to significantly reduce active power transients during synchronisation, specifically by minimising the peak's absolute value. It achieves this by integrating the design of the PI controller with the derivative droop on the primary control of grid-forming converters. Additionally, the algorithm addresses practical implementation challenges, such as communication delays and laboratory validation, factors often overlooked in existing approaches.

Table 1
Comparison of existing approaches for synchronising MGs. "**C**" means "consensus-based algorithm", "**SSA**" "small-signal stability analysis", "**P**" "method to reduce active power during transients", "**D**" "communication delays considered" and "**Lab**" "experimental validation".

Reference	C	SSA	P	Synch. method	D	Lab
[4]				PI + LPF		
[5]				MPC	✓	
[13]	✓			Fuzzy logic control		
[9]	✓	✓		PI control		
[10]	✓		✓	PI + LPF		
[11]	✓			Integral control		
[12]	✓		✓	PI + saturation		
This paper	✓	✓	✓	PI + deriv. droop	✓	✓

PI: proportional-integral, LPF: low-pass filter, MPC: model predictive control

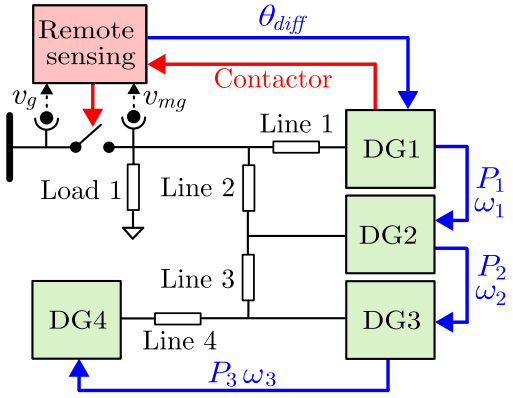

Fig. 1. Electrical and control system diagram of the MG studied in this work. Four DGs with a decentralised secondary controller.

The rest of the paper is organised as follows. An overview of the application is presented in Section 2, together with the main control and modelling tools used in the paper. Then, the design of the secondary controller in the presence of communication delays is presented in Section 3. Subsequently, the power flow analysis is presented in Section 4. The analytical results are presented in Section 5 and the experimental validation in Section 6. The proposed algorithm has been validated in a large system consisting of 69 buses, which includes seven grid-forming converters and primarily resistive lines in Section 7. Finally, conclusions are drawn in Section 8.

2. Application overview

2.1. System description

Fig. 1 shows the electrical and control diagrams of the MG studied in this work. It can work either connected to (closing a contactor) or disconnected from the main grid. Generation in the MG consists of four DGs that are interfaced with the grid by using voltage-source converters (VSCs) with LCL filters. The voltage at the connection point (v_{mg}) and the main grid voltage (v_g) are measured remotely, and the angle difference between them (θ_{diff}) is calculated and sent only to $DG1$. Each DG (DGi) has a grid-forming controller consisting of an outer voltage vector controller, an inner current vector controller (both in dq coordinates), a virtual impedance, and frequency and voltage droops [22]. On top of these controllers, a secondary active power-frequency controller is used to generate the output frequency set point for each DG. When the MG is connected to the grid, a secondary controller is used to control the power exchanged by the microgrid

with the grid. When the MG is working in island mode, the secondary controller seeks a consensus among the DG output frequencies and their share of active-power supply. In addition, when required, it synchronises the MG with the main grid. This controller does not require centralised processing of information but only communication between neighbours [23,24].

Each DG is considered as an "agent" whose outputs (P_i and ω_i in the figure) are calculated based on its local measurements and the information received from its neighbours exclusively. The received variables are the filtered active power multiplied by the droop gain, $mp_i P_i$ and the output frequency ω_i, all in per unit values, for all agents except the leader. The leader receives a power set point or the voltage measurement of the grid, depending on whether it tracks the injected power (after synchronisation) or attempts to synchronise with the grid.

2.2. Graph theory and consensus algorithms for MGs

The topology of a MG can be explained with a graph $G_r = (V, E)$, where there are N DGs (DGi) at the vertices (or nodes) of the graph grouped in V, and the edges of the graph, grouped in E, connect pairs of nodes. Each element of E is represented by the pair of nodes connected by the edge (DGi, DGj). A connection between two nodes means that information travels between them, and although bidirectional communication is possible in graphs, this paper assumes that information travels only from the first element of the pair to the second one. The use of bidirectional communication in the context of this paper is of interest for further research. In this specific situation, G_r is called "digraph" or "directed graph", and it is commonly used to model directed communication among DGs. All nodes DGj connected with DGi are its neighbours. Some of them will inform DGi while some others will receive information from DGi. The digraph is "simple" if no pair (DGi, DGi) belongs to E and there are no multiple edges between nodes. For a more detailed explanation of graph theory, see [25].

2.3. Droop control and consensus final value

For each DG (DGi) in the graph G_r, its droop control is formulated as [26]:

$$\omega_i(t) = \omega_i^*(t) - m_{Pi} P_i(t) - m_{Di} \frac{dP_i(t)}{dt}, \tag{1}$$

where subscript i refers to the DG number, $\omega_i(t)$ is its output frequency, $\omega_i^*(t)$ is its set point, $P_i(t)$ is the measured output power, m_{Pi} is the droop coefficient and m_{Di} is the derivative droop coefficient. To avoid noise amplification and unwanted interactions, the derivative droop is implemented as suggested in the literature [26], i.e., the angle of the output voltage space vector is imposed rather than the output frequency:

$$\omega_i(t) = \omega_i^*(t) - m_{Pi} P_i(t), \tag{2}$$

$$\theta_i(t) = \int \omega_i(t) dt - m_{Di} P_i(t). \tag{3}$$

A directed tree in a digraph is a subset of nodes connected by directed edges without cycles. If the tree is rooted, there is a node i designated as the root in which

$$d_i = \sum_j a_{ij} = 0 \tag{4}$$

where $a_{ij} = 1$ if the pair $(DGj, DGi) \in E$ and $a_{ij} = 0$ if the pair $(DGj, DGi) \notin E$. Therefore, the root node does not receive information from any other node. The value d_i is called the "in-degree" of node i. If one can reach every node of the graph from a designated root following the directed edges, the tree is called "spanning tree".

The frequency set point for each DG in the MG can be calculated by solving the following differential equation:

$$\frac{d\omega_i^*(t)}{dt} = -c_f \sum_{j \in N_i} a_{ij} \left[\omega_i^*(t) - \omega_j^*(t)\right], \quad i \neq k, \tag{5}$$

where c_f is the secondary control gain, controlling the speed of the secondary control and $j \in N_i$ if $(DGj, DGi) \in E$. In other words, DGj sends information (the value of ω_j^*) to DGi and constants a_{ij} are the weights given to the edge (DGj, DGi). In this work, $DG1$ takes the leader's role.

Ref. [23] shows that the leader DG in a microgrid must be the root of a spanning tree of the digraph. The calculation of the frequency of the leader is addressed in Section 2.5 for resynchronisation, and in Section 2.6 for grid-connected mode. For practical reasons (e.g., more visibility of variables, possibility to change droops, etc.), the controller is implemented replacing the steady-state droop characteristic (1) in the consensus algorithm (5):

$$\frac{d\omega_i^*(t)}{dt} = -c_f \sum_{j \in N_i} a_{ij} \left[m_{Pi} P_i - m_{pj} P_j\right] - c_f \sum_{j \in N_i} a_{ij} \left[\omega_i(t) - \omega_j(t)\right], \quad i \neq k. \tag{6}$$

If the graph has a spanning tree, the DGs will eventually reach a consensus [23]:

$$\omega_1^*(t = \infty) = \cdots = \omega_N^*(t = \infty). \tag{7}$$

Therefore, the whole MG will reach the same frequency value in steady state. In this work, $DG1$ (the one that receives the information from the point of connection to the main grid), will force the value of $\omega_1^*(t = \infty)$. Fig. 2 shows a detailed diagram of the primary and secondary controllers implemented for each DG to manage active power.

2.4. Steady-state operation

In steady state, the frequency and frequency set points of all the DGs will be the same and using (1):

$$\omega_1(t = \infty) = \cdots = \omega_N(t = \infty), \tag{8}$$

$$m_{P1} \cdot P_1(t = \infty) = \cdots = m_{PN} \cdot P_N(t = \infty). \tag{9}$$

which means that the pair DGi and DGj will work with the same output frequency and will share the power demand according to:

$$P_j(t = \infty) = \frac{m_{Pi}}{m_{Pj}} P_i(t = \infty). \tag{10}$$

2.5. Synchronisation with the main grid

The synchronisation with the main grid is considered complete when the amplitude, phase and frequency of the voltages at both sides of the grid contactor are the same. In this paper, voltage amplitude differences are not addressed, although this topic is interesting for further research. Without loss of generality, $DG1$ is also selected as the leader of the synchronisation process. $DG1$ can change its frequency set point (ω_1^*) as [10]:

$$\omega_1^*(s) = \omega_{1,0}^* + \overbrace{\left(K_{PS} + \frac{K_{IS}}{s}\right) \theta_{diff}(s)}^{\Delta\omega_1^*(s)}, \tag{11}$$

where s is the Laplace variable. To simplify the notation, the same symbol will be used for signals in the time and the Laplace domains (e.g., $\omega_1^*(s)$ and $\omega_1^*(t)$). The constant $\omega_{1,0}^*$ is the frequency set point of $DG1$ before switching the controller on, and K_{PS} and K_{IS} are the parameters of a PI controller. The term $\theta_{diff}(s)$ is the difference between the angles of the grid voltage space vector ($\vec{v}_g(t)$) and the MG voltage space vector at the connection point ($\vec{v}_{mg}(t)$). Space vectors are defined using dq components on a synchronously-rotating frame (i.e., $\vec{v}(t) = v_d(t) + jv_q(t)$) and the angle difference is calculated as follows:

$$\theta_{diff}(t) = \theta_g(t) - \theta_{mg}(t) = \text{ang}(\vec{v}_g(t) \cdot \left[\vec{v}_{mg}(t)\right]'), \tag{12}$$

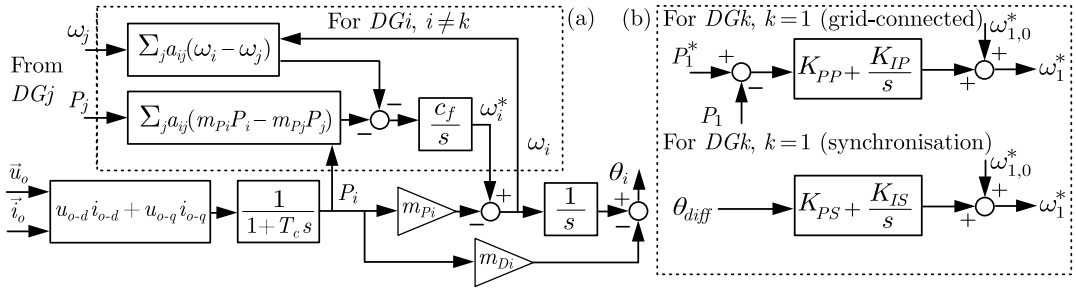

Fig. 2. Primary and secondary controller of a DG. In (a), for any DG except the leader (k). In (b), for the leader ($k = 1$ in this work).

where $\theta_g(t)$ and $\theta_{mg}(t)$ are the angles of $\vec{v}_g(t)$ and $\vec{v}_{mg}(t)$ with respect to the d axis, respectively. The symbol $'$ indicates "complex conjugate". Note that (12) can be calculated in any reference frame since the angle between space vectors is not affected by the reference frame selection.

When the MG and the main grid are synchronised, $\vec{v}_g(t)$ and $\vec{v}_{mg}(t)$ will rotate synchronously and $\theta_{diff}(t)$ will be zero.

2.6. Tracking of power set points

The MG can follow active power set points by adding a PI controller to the power injected by the leader ($DG1$):

$$\omega_1^*(s) = \omega_{1,0}^* + \overbrace{\left(K_{PP} + \frac{K_{IP}}{s}\right)}^{\Delta\omega_1^*(s)} (P_1^*(s) - P_1(s)), \tag{13}$$

where K_{PP} and K_{IP} are the PI controller parameters, and $P_1^*(s)$ is the active power set-point of $DG1$. In steady state, the active power injected by the leader will be equal to its set point, and the output power of the rest of the DGs can be easily calculated with (10). Neglecting losses, the total power injected into the grid is:

$$P_g(t=\infty) = \sum_{i=1}^{N} \frac{m_{Pi}}{m_{Pj}} P_i(t=\infty). \tag{14}$$

If accurate power control is needed, the total power injected to the grid can be measured and sent to $DG1$, to correct $P_1^*(s)$ in (13).

3. Synchronisation controller design

3.1. Dynamic equivalent of the consensus algorithm

To understand the dynamic relation between the frequencies of DGs, the Laplace transform of the frequency set-point of DGi in (5) must be calculated:

$$\omega_i^*(s) = -\frac{c_f}{s} \sum_{j \in N_i} a_{ij}\omega_i^*(s) + \frac{c_f}{s} \sum_{j \in N_i} a_{ij}\omega_j^*(s). \tag{15}$$

Notice that, in Fig. 1, only one DG sends information to any given DGi and that $\sum_{j \in N_i} a_{ij} = 1$ (i.e., there is only one interconnection per DG). Therefore, (15) is simplified to:

$$\omega_i^*(s) = \frac{1}{s/c_f + 1}\omega_j^*(s). \tag{16}$$

This first-order system relates the frequency set points of connected DGi and DGj and proves that frequency set points will not be uniform across the MG during transients. Moreover, if the transient response of (16) is slow, the performance of the secondary controller will deteriorate. The expression in (16) is used in the remainder of this work instead of (15) because the former is correct for the MG topology studied in this work.

3.2. Modelling and effect of communication delays

If communication delays exist, each agent i sees its neighbours' frequency (the ones to follow) with a delay. Therefore, Eq. (16) must be written as:

$$\omega_i^*(s) = \frac{1}{s/c_f + 1} \underbrace{e^{-sT_d}\underline{\omega}_j^*(s)}_{\omega_j^*(s)}, \tag{17}$$

where $\underline{\omega}_j^*(s)$ is the frequency before applying the communication time delay T_d between the two DGs (alternative models can be found in [27], for example). A large time delay can lead to an unstable consensus secondary control [14].

The graph structure is maintained throughout this study to simplify explanations because the choice of the graph affects the system dynamics and its robustness against changes in communication delays [24]. In addition, even though small communication delays will not jeopardise the stability of the consensus algorithm, its performance will deteriorate. In particular, for MGs formed by GFo-VSCs, delays greatly modify the power injection requested from each DG to synchronise the MG because the droop control of GFo-VSCs described in (1) guarantees that DGs share active-power disturbances proportionally to their droop coefficients, but only if the frequency set points of all the DGs are the same. However, in decentralised secondary controllers, this is only true when the steady state is reached. Consequently, if DGs temporarily have different frequencies (as is the case if communication delays are considered), the angle difference between nodes would also change temporarily, producing unwanted active power transients. These transients may lead to unwanted disconnections of DGs or protections tripping, although they can be reduced if changes in the synchronisation angle are made slowly. This issue has been tackled by limiting the rate of change of the frequency set point in [10], and by limiting the frequency change given by the PI controller in [12]. Alternatively, the PI controller speed can be adapted, leading to a more systematic design. In Section 4, a simple test case illustrates the mentioned consequences of communication delays on synchronisation dynamics by means of time-domain simulations of a simplified model. The usage of this model is introduced and justified in the following subsections.

3.3. Power exchanged between two DGs

The instantaneous power flow between two DGs (DG_i and DG_j) interconnected by a mainly-inductive electrical line can be approximated as follows [6]:

$$P_{ij} = \frac{v_i v_j}{X_{ij}} \sin\delta_{ij} \approx \frac{v_i v_j}{X_{ij}} \delta_{ij}, \tag{18}$$

where v_i and v_j are the modules of the DGs output voltages, X_{ij} is the impedance between them calculated for the nominal frequency, and δ_{ij} is the angular difference between the DG output voltages. In practice, δ_{ij} is small and $\sin\delta_{ij} \approx \delta_{ij}$. If the line between DGs is not mainly inductive or its impedance is large, a virtual impedance can be used to adjust the output impedance of DGs [28].

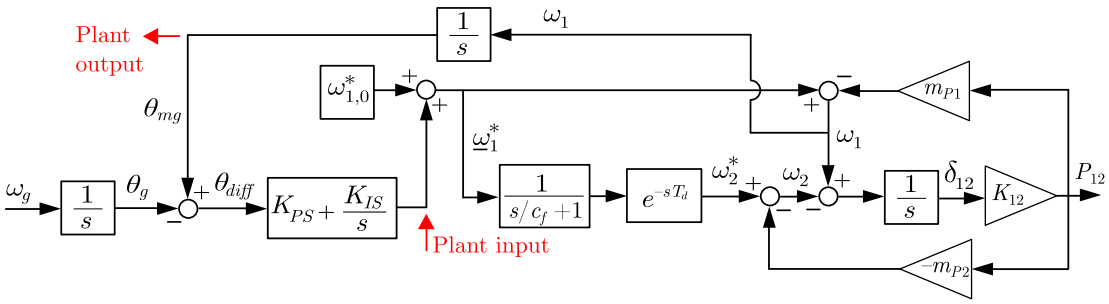

Fig. 3. Block diagram representing the dynamic model of the agent-based secondary controller applied in this work.

Differentiating (18) and assuming that the output voltage of the DGs, v_i and v_j, and the line impedances X_{ij} are constant, gives:

$$\frac{dP_{ij}}{dt} = \frac{v_i v_j}{X_{ij}}(\omega_i - \omega_j). \tag{19}$$

which means that steady state without power oscillations (i.e., $dP_{ij}/dt = 0$) is only reached if $(\omega_i - \omega_j) = 0$.

3.4. A complete model of the synchronisation process

Fig. 3 depicts the synchronisation controller, the droop control, the power flow equations between DGs, the secondary controller and the communication delay. This diagram will be used to design the synchronisation controller, and each block within that diagram is explained in the remainder of this subsection using two DGs, namely $DG1$ and $DG2$, where $DG1$ is the leader. Notice that $DG1$ is the only agent that has access to the grid voltage measurements.

The output frequencies of the DGs can be calculated adapting (1) to $DG1$ and $DG2$:

$$\omega_1 = \underline{\omega}^*_1 - m_{P1} \cdot P_1 - m_{D1}\frac{dP_1}{dt}, \tag{20}$$

$$\omega_2 = \omega^*_2 - m_{P2} \cdot P_2 - m_{D2}\frac{dP_2}{dt}. \tag{21}$$

As the derivative droop has a very fast control action, one can assume that $dP_i/dt = 0$. In addition, the power flow between $DG1$ and $DG2$ can be modelled by setting $i = 1$ and $j = 2$ in (18), yielding (if $\delta_{12} \approx 0$):

$$P_{12} = \frac{v_1 v_2}{X_{12}}\sin\delta_{12} \approx \frac{v_1 v_2}{X_{12}}\delta_{12} = K_{12}\delta_{12}, \tag{22}$$

In Fig. 3, communication delays are modelled by using (17) with $i = 2$ and $j = 1$.

3.5. PI controller design

In this paper, open-loop frequency response techniques are used since they are well suited for high-order systems that include delays, as the one presented in Fig. 3. In that figure, the plant transfer function can be calculated as the equivalent system between the points labelled "Plant input" and "Plant output". For the design, it was deemed adequate to set the phase margin (ϕ_m) and the crossover frequency (ω_0) of the open-loop system from which the parameters of traditional PID controllers can be calculated analytically [29].

4. Power flow characterisation and control

4.1. Explanation of the case study

In this section, the active-power flow between two DGs (from $DG1$ to $DG2$) is investigated by using numerical simulations to understand the effect of the communication delay (T_d), and the phase margin (ϕ_m) and the crossover frequency (ω_0) of the angle-difference controller described in Section 3. The parameters used in the numerical simulation are written in Table 2. Calculations in the droop control have been carried out with and without the derivative term to highlight its importance.

Table 2
Parameters used in the simulation study in Section 4.

$v_1 = v_2 = 400$ V	$Z_{12} = j \cdot 2\pi 50 \cdot 20e^{-3}$ Ω
$\omega^*_{1,0} = \omega^*_{2,0} = 2\pi \cdot 49.5$ rad/s	$\theta_{diff} = \pi$ rad (initial)
$m_{P1} = m_{P2} = 2 \cdot 10^{-4}$ rad/s/W	

4.2. Characterising active power flow between DGs

(1) Effect of Phase Margin:
Figs. 4(a) and 4(c) show the synchronisation time and the peak of the active power flow between $DG1$ and $DG2$ when the MG is synchronised with the main grid, respectively. A constant time delay of $T_d = 30$ ms was considered. In both cases, the crossover frequency (ω_0) was modified between 0.5 and 1.5 rad/s, and the phase margin (ϕ_m) was modified between 50 and 80 degrees. In Fig. 4(a), the synchronisation time is calculated as the time needed to reach an angle difference (θ_{diff}) smaller than two degrees. Clearly, the synchronisation time can be reduced by increasing the crossover frequency and reducing the phase margin, but this will also increase the active-power flow during transients. The crossover frequency can be reduced as much as needed; however, the phase margin should be kept within adequate margins to avoid unwanted oscillations. In summary, a compromise between synchronisation speed and transient active-power flows must be accepted.

(2) Effect of Time Delay: Fig. 4(e) shows the peak of active power needed to synchronise $DG1$ and $DG2$ with the main grid, for different values of the communication delay and the crossover frequency. The phase margin (ϕ_m) was set to 60 degrees. Clearly, the active power peak increases together with the communication delay and the crossover frequency. Therefore, the design of the synchronisation controller should consider both the maximum expected communication delay and the maximum allowed active power peak. In this paper, since all the DGs are similar and there are no limitations in their primary energy source, the limit is established by the highest active power peak. From the analysis carried out in this section, it is clear that the active power peak during the synchronisation is the key issue to be considered in the synchronisation controller design. To reduce its impact on synchronisation dynamics, the next section proposes a method to reduce this active power peak during the synchronisation transient.

4.3. Reduction of transient active-power peak

As shown in the previous section, the ability of the secondary controller to limit the power during transients is quite limited. A possible solution is to design the primary controller to react faster to

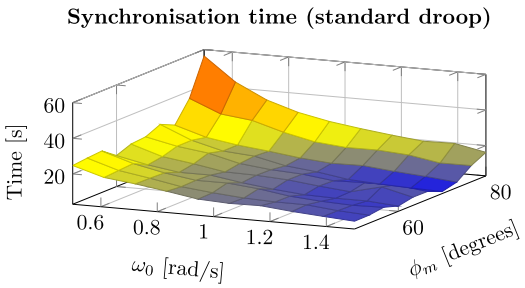

(a) Synchronisation time as a function of the open-loop phase margin and crossover frequency of the system. Standard droop.

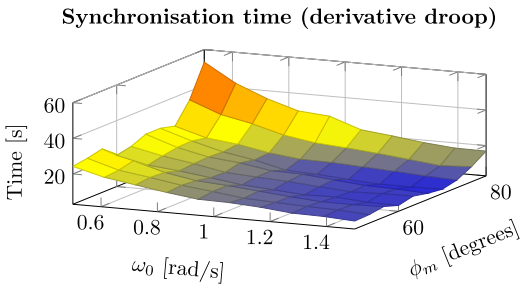

(b) Synchronisation time as a function of the open-loop phase margin and crossover frequency of the system. Derivative droop.

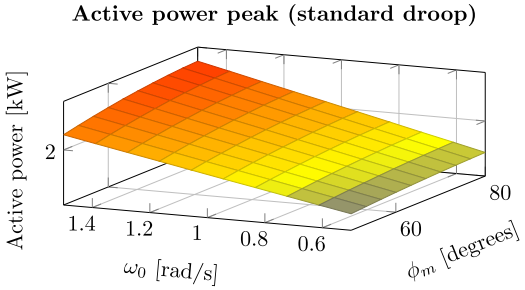

(c) Peak of the active power transient between DGs as a function of the open-loop phase margin and crossover frequency of the system. Standard droop.

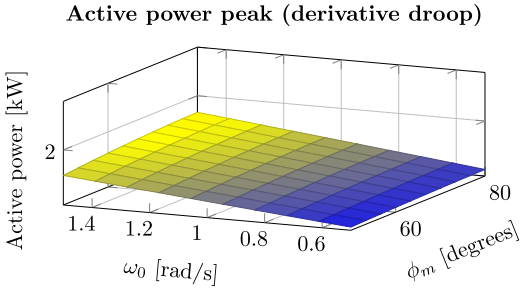

(d) Peak of the active power transient between DGs as a function of the open-loop phase margin and crossover frequency of the system. Derivative droop.

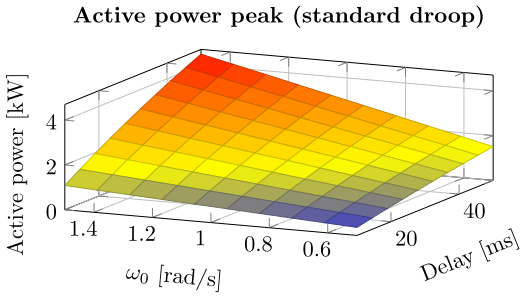

(e) Peak of the active-power transient between DGi and DGj, for different values of the communication delay (T_d) and crossover frequency (ω_0). Standard droop.

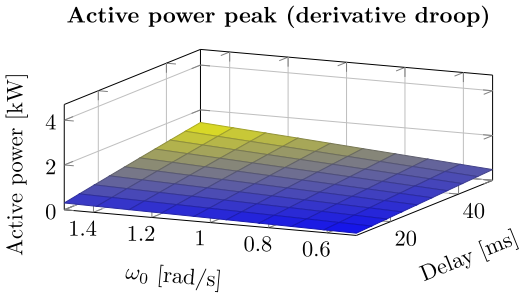

(f) Peak of the active-power transient between DGi and DGj, for different values of the communication delay (T_d) and crossover frequency (ω_0). Derivative droop.

Fig. 4. Fundamental study of the powerflow between two DGs.

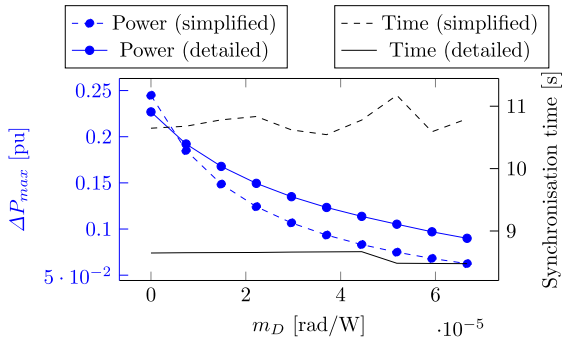

Fig. 5. (blue) Active power peak needed for synchronisation and (black) synchronisation time, for different values of m_D (dashed) Simplified and (solid) detailed MG model.

changes in the angle of the connection point. In a traditional droop control scheme, this can only be achieved by increasing the droop gain or the virtual impedance. However, the droop gain is typically selected according to the active power-frequency requirements, while the virtual impedance should be carefully selected to guarantee adequate dynamic performance of the DG. The derivative terms of the droop in (20) and (21) give an additional degree of freedom [26].

To understand the effect of the derivative droop term, the results obtained for the standard droop in Fig. 4(a),4(c) and 4(e), were replicated, including the derivative droop term, in Figs. 4(b), 4(d) and 4(f). A value of $m_D = 5.33 \cdot 10^{-5}$ was used (the details of how this value was selected are presented in the following section). In the results, the synchronisation time remains almost unaffected, while Fig. 4(d) shows that the active power exchanged between DGs was halved. In addition, Fig. 4(f) shows that the effect of the delay is greatly reduced.

Table 3
MG hardware and control parameters.

System parameters		
$V_n = 400$ V	$f_n = 50$ Hz	$R_{load} = 16\ \Omega$
$L_{line1} = 0.1$ mH	$L_{line2} = 0.4$ mH	$R_{line}/X_{line} = 0$
$L_{line3} = 0.092$ mH	$L_{line4} = 0.27$ mH	
DG hardware parameters		
$L_c = 1.5$ mH	$C_f = 8.8\ \mu$F	$L_o = 2.2$ mH
$R_c = 48$ mΩ	$R_f = 48$ kΩ	$R_o = 173$ mΩ
$f_{sw} = 10$ kHz	$f_s = 10$ kHz	$L_V = 10$ mH
Initial operating point		
$P_i = 2.502$ kW	$\omega^*_{i,0} = 2\pi 50$ rad/s	
$Q_i = 0.027$ kVAr	$v^*_i = 400$ V	
MG topology and communication definition		
$a_{i(i-1)} = 1\ \forall i \neq 1$	$a_{ij} = 0\ (\forall j \neq i-1)\ \vee\ i = 1$	
Primary control parameters		
$m_P = 2 \cdot 10^{-4}$ rad/(s·W)	$K_{PV} = 0.12$	$K_{PC} = 4.53$
$n_Q = 1 \cdot 10^{-4}$ V/VAr	$K_{IV} = 36.29$	$K_{IC} = 10600$
$m_D = 5.33 \cdot 10^{-5}$ rad/W	$T_c = 1.5$ ms	
Secondary control parameters		
$K_{PS} = 0.0155$	$K_{PP} = 2 \cdot 10^{-5}$	$T_d = 3.2$ ms
$K_{IS} = 0.0062$	$K_{IP} = 2 \cdot 10^{-4}$	$c_f = 30$

5. Further details of the case study and analysis

5.1. MG description and parameters

The MG presented in Fig. 1 was modelled in Simulink. The system parameters presented in Table 3 were used, where L_c is the converter-side inductance of the LCL filter (R_c is its resistance), C_f is the capacitor of the filter (R_f is its parallel resistance) and L_o is the output inductance of the filter (R_o is its resistance). The switching and sampling frequencies are f_{sw} and f_s, respectively. A traditional reactive droop (n_Q) with a LPF was used for the reactive power [30]. The internal current and voltage controllers are standard and include PI controllers with d-q dynamics decoupling terms [22]. The gains of the current controller are K_{PC} and K_{IC}, and the gains of the voltage controller are K_{PV} and K_{IV}. In addition, a virtual impedance (L_V) ensures adequate stability margins [31]. The information exchange between DGs is depicted in the left-top corner of Fig. 2.

For the LPF in (17), it was found that $c_f = \omega_{bw} \geq 30$ in (15) does not have a significative impact on the performance of the synchronisation controller, and this value was chosen for the implementation.

5.2. Effect of derivative droop term

Fig. 5 shows, in blue, the peak of the active power needed to synchronise the MG, and in black, the synchronisation time. Different values of the derivative droop term (m_D) were tested (see the horizontal axis). The results obtained for the simplified model presented in Section 3.2 are drawn with dashed lines while the values obtained with the detailed simulation are drawn with solid lines. Clearly, results are relatively similar. The active power peak is reduced by increasing m_D while the synchronisation time remains almost constant. This fact greatly simplifies the design of the derivative droop term, which can be selected before designing the secondary controller.

Fig. 6 shows the system eigenvalues of a linearised version of the complete MG model, when m_D increases. The angle of the eigenvalue ($\text{ang}(\lambda_i)$) is placed at the vertical axis while the absolute value ($\text{abs}(\lambda_i)$) is placed at the horizontal axis, in a logarithmic scale. For each complex pair, only the one with a phase between 90 and 180 degrees is plotted. In this representation, all the system eigenvalues fit in a single plot, and critical eigenvalues can be easily spotted. Notice that a pair of complex eigenvalues is unstable if the angle is less than 90 degrees, while a real

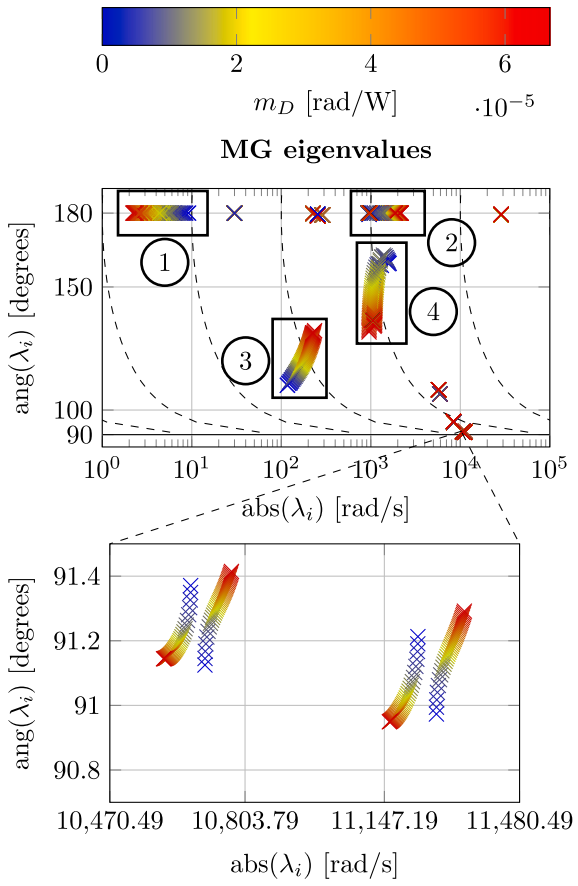

Fig. 6. Angle versus absolute value of the MG eigenvalues, for different values of m_D (see the text for explanations).

eigenvalue (placed at 180 degrees) tends to be unstable when travelling towards $-\infty$. The main eigenvalues are marked with numbers (from ⟨1⟩ to ⟨4⟩). The participation factor of each eigenvalue was calculated to understand to which variable it is linked to [30]. The eigenvalue ⟨1⟩ is real, and it approaches minus infinity when the m_D increases. It is mainly related to the integral of the frequency, which is directly related to the output of the PI controller used to synchronise the MG.

The eigenvalue ⟨2⟩ is real, while ⟨3⟩ and ⟨4⟩ are complex. These eigenvalues are mainly related to the output of the measurement filter (i.e., they are strongly affected by the droop and its derivative).

From these results, it can be concluded that an adequate value of m_D should guarantee that both ⟨3⟩ and ⟨4⟩ are placed in adequate positions.

Theoretically, the system eigenvalues are stable if $m_D \leq 6.7 \cdot 10^{-5}$ rad/W. To have a compromise between the location of ⟨3⟩ and ⟨4⟩ (damping factors of around 0.5), a value of $m_D = 5.33 \cdot 10^{-5}$ rad/W was selected.

A zoom on the pair of complex eigenvalues related to the resonance of the LCL filter is included in Fig. 6. Even though the phases of these eigenvalues are close to 90 degrees, these eigenvalues should be damped by the parasitic resistances of the DGs and the electrical interconnections, in a practical implementation [32]. Droop coefficients m_p and n_q are designed considering the nominal power of the converters, to have desired active and reactive power sharing of disturbances. In this work, all converters are the same size, so the droop coefficients are equal for all converters. The value of m_p and n_q can be designed with the procedure described in [33]. For example, m_p is designed similarly to m_D, with eigenvalue analysis.

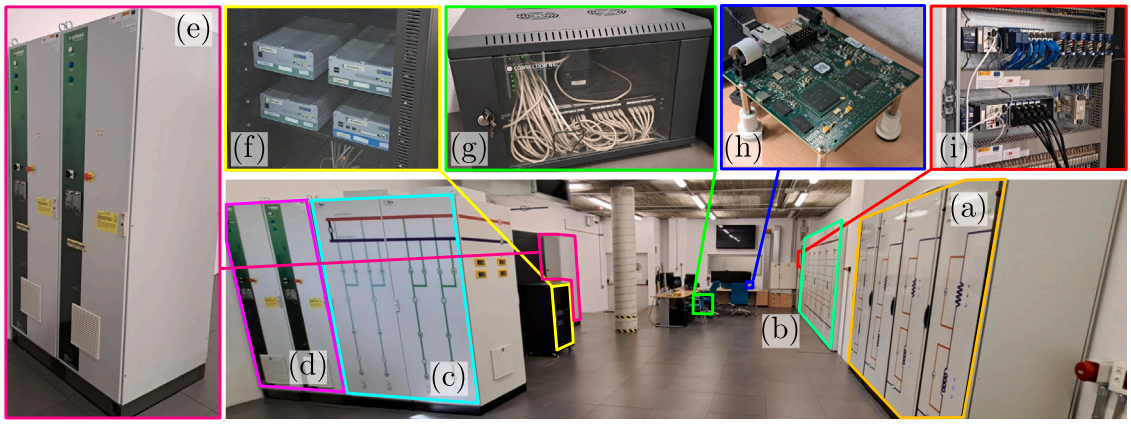

Fig. 7. Pictures of the elements of the laboratory. (a) Line impedances, (b) AC busbars, (c) DC busbars, (d) 75 kVA VSCs, (e) 15 kVA VSCs, (f) real-time computers, (g) communication network switch, (h) single-board RIO and (i) two compactRIO.

6. Experimental validation

6.1. Laboratory description

The theoretical results of previous sections were validated in the laboratory facilities of IMDEA Energy (see Fig. 7). Four VSCs with LCL filters were used to emulate the DGs (marked in green as $DG1$, $DG2$, $DG3$ and $DG4$). Meanwhile, the main grid was emulated with a 75 kVA VSC with an LCL filter. The communication between DGs is implemented in a *single-board RIO* platform which takes all the information from the real-time PCs that control the VSCs, re-routes it, and sends it back to the selected real-time PCs. In this way, it is possible to define a communication graph and then implement it via the *single-board RIO*.

6.2. Experimental results

First of all, the delay between DGs was measured. using the real-time PC1 (the one controlling $DG1$ and $DG2$). Fig. 8 shows a histogram representing the measurements of the communication time delay between $DG1$ and $DG2$. The delay has a stochastic component, similar to a normal distribution with a mean value of 3.2 ms. As shown in [27], the mean value can be used to analyse the performance of control loops if the delay is not too big.

Fig. 9(a) shows the experimental results obtained. Initially, the MG was operating as an island and θ_{diff} was increasing steadily. At the instant "Sync", the synchronisation controller was activated. After this moment, the angle difference (θ_{diff}) approaches zero and reaches the steady-state in ten seconds, approximately. The synchronisation process does not require an excessive value of active power thanks to the use of the derivative droop.

Once the MG was synchronised with the grid, the grid contactor was closed (at the instant "Close") and there is only a small transient in the active power and in the frequency (almost unnoticeable) because the MG and the main grid were accurately synchronised.

Finally, when the MG was connected to the main grid, a step change of 4 kW was applied to the set point of the MG active power (i.e., $\Delta P_1^* = 4/4 = 1$ kW for $DG1$). The results show that all the DGs rapidly change their active power injection and follow the set point value, accurately.

The experimental results are compared in this section with two simulation models, one implemented using the Simscape Electrical toolbox in Simulink that includes the switching of converters and an own developed Simulink tool that includes an average modelling of the converters, described in [34]. Details on the models are included in [35]. Fig. 9(b) compares the experimental results with the results obtained from the switched and the averaged simulation models. The events of the test are the same as those used in Fig. 9(a). The figure

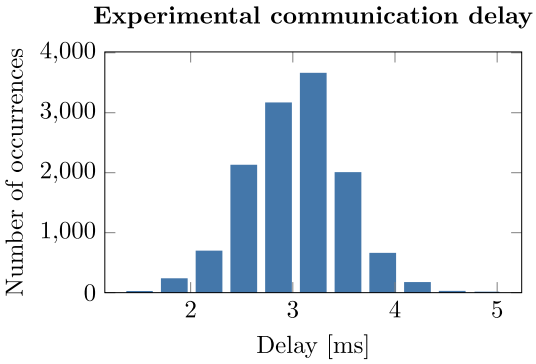

Fig. 8. Histogram of the experimental measures of the communication delay between $DG1$ and $DG2$ in the laboratory.

shows the active power output of $DG1$, its frequency, and the angle difference (θ_{diff}). Simulation and experimental results are very similar. However, in the experimental test (in blue), the power needed to synchronise the MG is slightly higher than in the theoretical models, probably because the real system has additional losses that were not considered in the simulation models (e.g., switching losses, etc.). Nevertheless, the shape of the transients was almost identical, indicating that simulation models are useful tools to predict the dynamic behaviour of the MG.

7. Large case study

This section describes the application of the proposed synchronisation method to a modified version of the IEEE 69 test system to demonstrate the scalability of the proposed algorithm. One of the advantages of decentralised multi-agent control is that the control rules can still be applied to systems with more agents. Therefore, the same control will be applied in the large test system, only ensuring a spanning tree still exists. Fig. 10 includes the single-line diagram of the test system. The MG will be connected to the main grid (after synchronisation) with a controllable switch connected at bus 33. For this test case, a communication time delay of 10 ms was considered between all converters. The synchronisation control structure and parameters are the ones used for the case with four converters.

The case study represents a radial distribution system that consists of 69 buses and 68 branches. The total system load is 3.802 MW and 2.694 Mvar. GFo-VSCs DGs 1–7 are connected at buses 1, 11, 21, 31, 41, 51 and 61, respectively. The bases and parameters used for the test system and GFo-VSCs can be found in Table 4. Compared

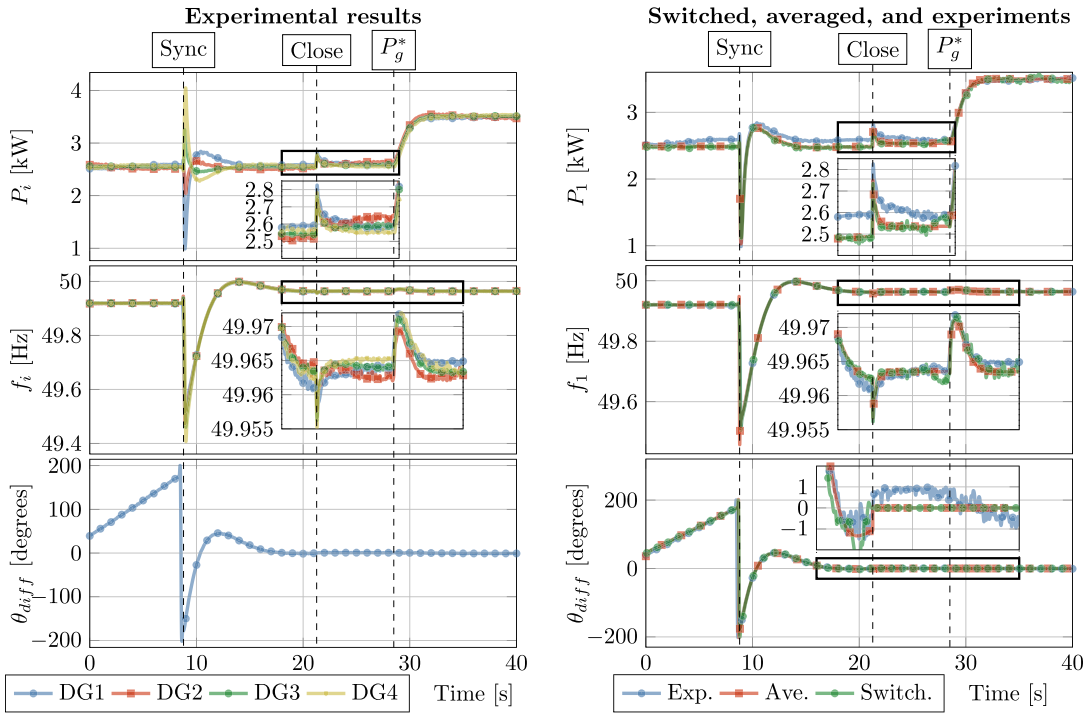

(a) Experimental results. Resynchronisation and grid-connected control modes. From top to bottom, active power (P_i), frequency (f_i) and angle difference (θ_{diff}).

(b) Comparison of the switched model, the averaged model and the experimental results. From top to bottom, active power (P_1), frequency (f_1) and angle difference (θ_{diff}).

Fig. 9. Comparison of the switched model, the averaged model and the experimental results.

Table 4
Parameters used for the simulation of the modified IEEE 69 bus test system.

GFo-VSC			
m_P	$1 \cdot 10^{-7}$ rad/(s·W)	n_Q	$1 \cdot 10^{-4}$ V/VAr
R_f	0.048 Ω	L_f	1.5 mH
C_f	66.32 μF	R_{cf}	48 kΩ
R_c	0.048 Ω	L_c	1.5 mH
K_{PV}	0.02	K_{IV}	0.2
K_{PC}	50	K_{IC}	500
F_i	1	LPF_{const}	0.01 s
Sec. control parameters and bases			
c_f	1	c_v	1
f_{base}	50 Hz	S_{base}	3 MVA
delay (T_d)	10 ms	$V_{nom} = V_{base}$	12.6 kV
β	0	B	1
$g_1 = 1$	$g_i = 0 \; \forall \; i \neq 1$	$a_{ij} = 1 \; \forall \; i \neq 1, \; j = i - 1$	
ω_{ref}	1 pu	v_{ref}	1 pu
K_{PS}	0.0155	K_{IS}	0.0062
Initial operation point ($i \in [1-7]$)			
P_i	532.54 kW	Q_i	374.82 kVAr

to the laboratory case, the parameters of the inner controllers of the GFo-VSCs differ due to differences in the electrical elements of the system. The delay is increased to have a more realistic value for larger systems. However, it should be noted that the synchronisation control parameters remain the same to validate the plug-and-play nature of the proposed approach. The communication graph used for this test case study is radial, as the previous one, from DG1 to DG7. The default communication delay among converters is set to a constant value of 10 ms. The delay is modelled using a third-order Padé approximation in linearised models.

The synchronisation process is divided into the following stages:

1. **Secondary control activation**: At $t = 10$ s, the secondary control is activated. This guarantees active-power sharing among converters.
2. **Synchronisation starts**: At $t = 30$ s, the synchronisation control is activated. This changes the frequency set point of the leader DG.
3. **Closing the contactor**: After the synchronisation, the controllable switch between the microgrid and the main grid is closed. This occurs when the synchronisation thresholds are met.
4. **Increasing the active-power injection to the main grid**: 10 s after the close of the contactor, the microgrid is asked to inject 5.25 MW of active power into the main grid.

Fig. 11 shows the results of the simulation of the synchronisation process. Clearly, the results obtained are similar to those in the case of four grid-forming converters. The synchronisation implies an active power transient limited by the design of the proposed control, the angle difference is driven to 0 in a few seconds, avoiding big transients in the connection to the main grid, and the microgrid successfully injects power into the main grid after the connection with the selected active and reactive power sharing among converters. The key difference in this result is that the secondary control in islanded operation before the synchronisation maintains the frequency in its nominal value while guaranteeing active power sharing between converters.

7.1. Consideration of the voltage amplitude difference

The proposed algorithm is mainly designed to consider frequency and angle synchronisation because, in the studied scenarios, the voltage was very similar in the MG and the main grid. Therefore, the voltage

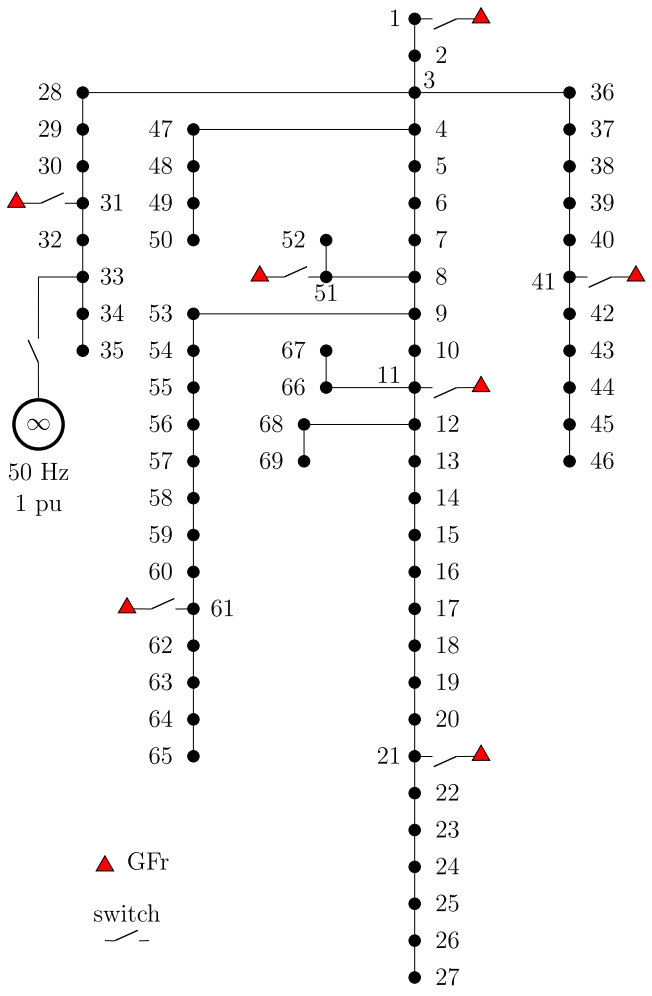

Fig. 10. Single-line diagram of the modified version of the IEEE 69 bus test system.

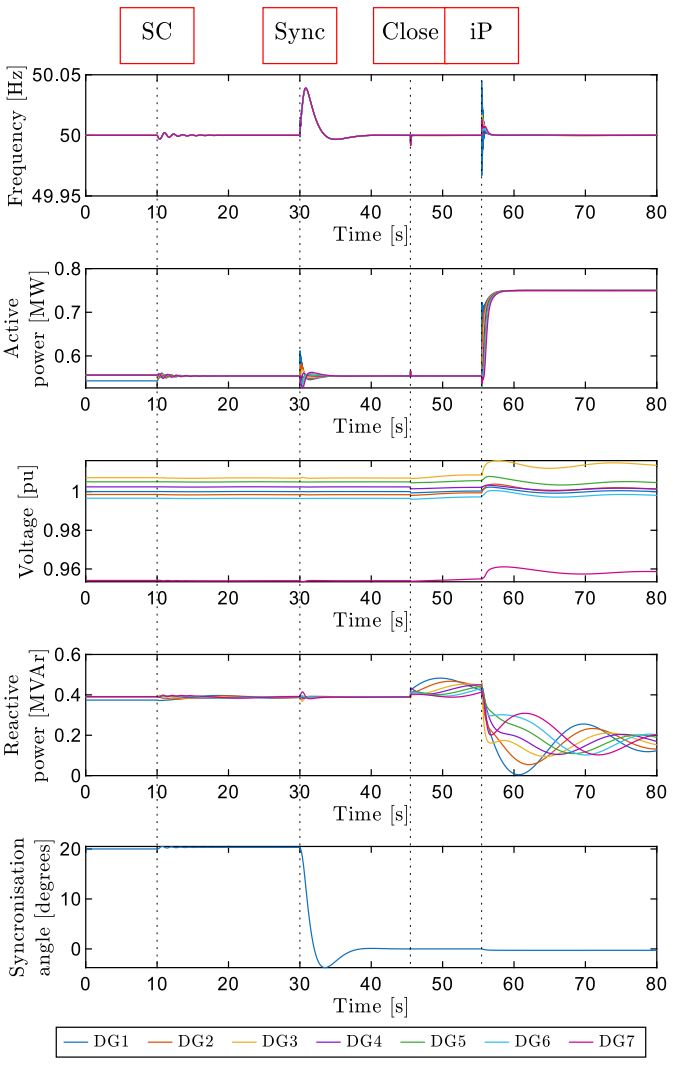

Fig. 11. Simulation results of the synchronisation of the IEEE 69 bus test system to an infinite grid with the proposed control.

difference was not the main concern. However, to test the proposed algorithm in order to work in the case of a voltage amplitude difference, the algorithm must include another PI controller. Similarly to the proposed angle synchronisation, the voltage amplitude difference is tracked and controlled by a PI controller in the synchronisation angle. The proportional and integral control gains for this PI controller are 1 and 20, respectively. The output of this synchronisation controller, initialised to 1 pu, is the voltage reference that the leader DG must track in its voltage secondary control. Note that this PI control must be deactivated when the MG is required to inject power to the main grid.

Fig. 12 includes the simulation results of including that PI controller, compared to the previous case without it.

As shown in the figure, the performance of the algorithms is very similar, except for the voltage amplitude difference, controlled to 0 during the synchronisation in case 2, and the reactive power transient that occurs in case 2 due to the control of that voltage difference. The small transient in reactive power at the moment of the connection is avoided in case 2 thanks to the voltage amplitude control.

7.2. Effect of the limitation of available primary energy resource

In this work, we have not modelled the primary energy resource of the converters. For the simulations, the converters are modelled as ideal controlled voltage sources. For the experimental setup, the IMDEA lab utilises an AC/DC rectifier as the primary source, connected to the mains via a transformer with adjustable taps, which maintains a constant DC voltage when active power is injected from the converter into the AC grid. In any case, our hypothesis is that the primary resource and its control respond sufficiently fast that DC link voltage variations do not impose any barrier. However, the possible active power limitation imposed by the primary energy source grid-forming converter must be considered for a realistic scenario. To prove the performance of the proposed algorithm, this section includes the consideration of this limitation. In this section, to achieve a larger active power peak and observe the limitation effect clearly, both gains of the proposed synchronisation PI control are multiplied by a factor of ten. The limitation of available energy from the primary resource is implemented by an active power limitation with a fast PI controller acting on the frequency of the converter when saturated, as described in [36].

The simulation results on the effect of this limitation are shown in Fig. 13.

As shown in the Figure, the active power peak of converter DG1 is reduced because it is not able to reach that power due to the limitation. This has the effect of slightly slowing the synchronisation because DG1 (the leader) is unable to follow the frequency set point given by the PI controller until it is limited. Except for this detail, the performance of the control is very similar, validating its robustness to this transient limitation.

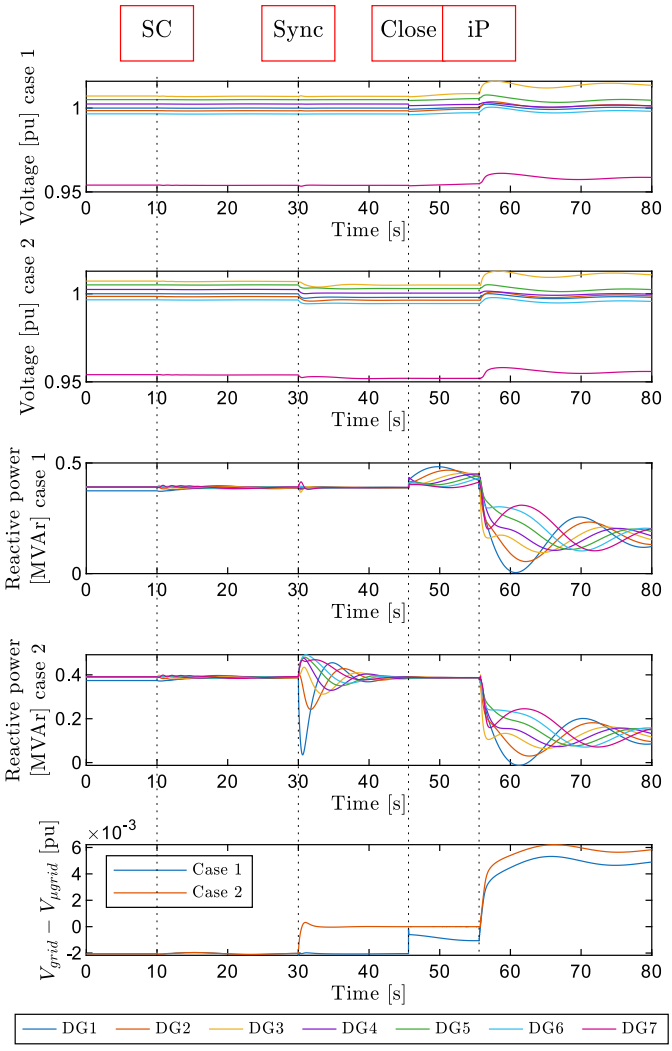

Fig. 12. Voltage, reactive power and voltage amplitude difference (V_{grid} – $V_{microgrid}$) comparison between case 1 (no amplitude difference control) and 2 (amplitude difference control).

All these results apply to a microgrid composed of grid-forming converters. In the case of including grid-following converters, the consensus control can still be applied for the secondary control layer. Using the secondary control described in [6], the grid-following converters can be incorporated in the active and reactive power sharing of the control. However, they do not include consensus control on frequency. Including grid-following converters would have a similar performance to that of having only grid-forming converters, even reducing the active-power peak during the synchronisation transient because the grid-following units control their injected current.

In the event of the loss of a communication link, as stated in consensus theory, consensus cannot be guaranteed if no spanning tree exists in the communication graph. Since the synchronisation control includes a PI agent, synchronisation would still occur, but with worse performance in terms of active and reactive power sharing. Instead, there will be active and reactive power sharing between two different groups of converters, corresponding to the two connected subgraphs in the secondary control communication network. In this scenario, a meshed communication network is more robust, as it can still maintain a spanning tree in the event of losing a communication link, thereby ensuring active and reactive power consensus. The proposed algorithm can be applied seamlessly to meshed communication networks.

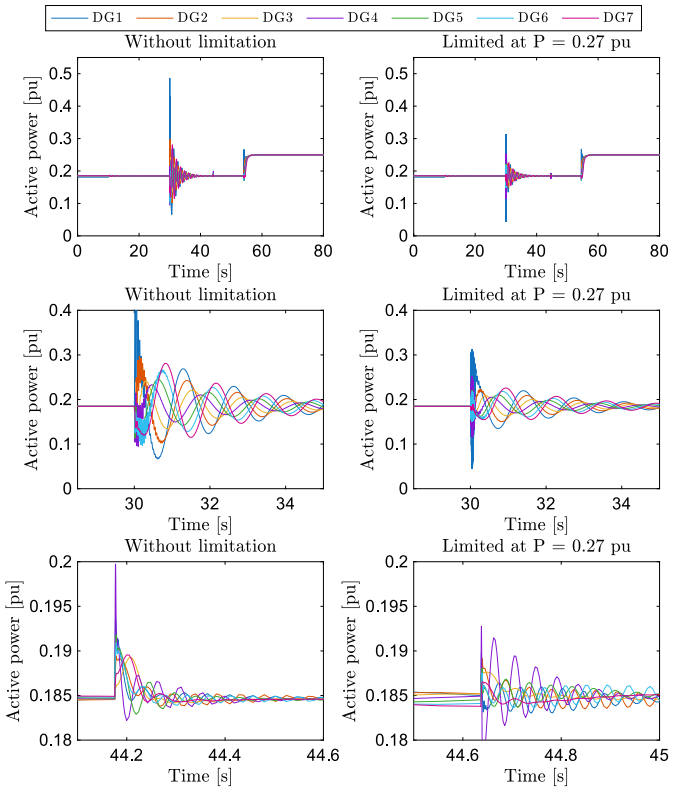

Fig. 13. Effect on the limitation of available active power from the primary energy resource. The first zoomed region corresponds to the synchronisation transient, and the second zoomed region corresponds to the connection transient.

8. Conclusion

In this paper, a multi-agent secondary controller was proposed and investigated to synchronise MGs with the main grid. Two main effects of the communication delays have been studied: their impact on the system stability and on the active power required for the resynchronisation. The delays were considered at the design stage of the PI controller so the transient response of the MG was adequate and a derivative term in the droop of DGs was proposed to reduce the active power peaks during transients. The main findings were validated by using numerical simulations and laboratory experiments performed in a realistic environment.

The analytical results showed that communication time delays can greatly affect the power needed to synchronise the MG. Although it was found that this effect can be reduced by using a faster secondary controller, a derivative droop term together with an adequate design of the secondary controller was proved to be a more effective strategy. In this way, it is possible to decrease several times the power needed to resynchronise the MG while making the system less dependent on communication time delays. The detailed small-signal model revealed the impact of the derivative droop term in different eigenvalues of the MG, and a trade-off between the damping of all of them was established. The experimental results obtained in the laboratory were very similar compared to the numerical simulation results and only some small deviations in the power needed to perform the synchronisation were observed.

These results underscore the practical relevance of the proposed controller, demonstrating its robustness and applicability to real microgrids operating over industrial communication infrastructure with significant communication time delays.

The proposed algorithm is validated in a large system of 69 buses with seven grid-forming converters and mainly resistive lines. The algorithm is also validated in the case of limited available energy from the converters and considering control of the voltage amplitude difference between the microgrid and the main grid.

CRediT authorship contribution statement

Andrés Tomás-Martín: Writing – original draft, Visualization, Software, Methodology, Formal analysis, Data curation, Conceptualization. **Javier Roldán-Pérez:** Writing – review & editing, Visualization, Validation, Supervision, Project administration, Methodology, Funding acquisition. **Njegos Jankovic:** Writing – review & editing, Visualization, Validation, Resources. **Sauro Yagüe:** Methodology, Formal analysis, Conceptualization. **Lukas Sigrist:** Writing – review & editing, Validation, Supervision, Project administration, Funding acquisition. **Aurelio García-Cerrada:** Writing – review & editing, Visualization, Supervision, Project administration, Methodology, Funding acquisition, Conceptualization.

Declaration of competing interest

The authors declare that they have no known competing financial interests or personal relationships that could have appeared to influence the work reported in this paper.

Acknowledgements

This work has been partially financed through the research program S2018/EMT-4366 PROMINT-CAM on Smart Grids of Madrid Government, Spain, with 50% support from the European Social Fund, and through grant MIG-20201002 funded by *Centro para el Desarrollo Tecnológico Industrial (CDTI)*, Spain and supported by *Ministerio de Ciencia e Innovación*, Spain. The simulation tool used for the average model and small-signal analysis has been developed through Grant TED2021-130610B-C22 funded by MICIU/AEI/10.13039/501100011033, Spain and by European Union NextGenerationEU/PRTR.

Data availability

Data will be made available on request.

References

[1] Marnay C, Chatzivasileiadis S, Abbey C, Iravani R, Joos G, Lombardi P, Mancarella P, von Appen J. Microgrid evolution roadmap. In: 2015 international symposium on smart electric distribution systems and technologies (EDST). Vienna, Austria: IEEE; 2015, p. 139–44.
[2] Rai I, C S. Microgrid and grid synchronization: A critical analysis of challenges and opportunities. Electr Power Syst Res 2025;242:111434.
[3] Acharya S, Vijaya Kumar D. Frequency stabilization and synchronization between grid and AC microgrid. Electr Power Syst Res 2024;228:110045.
[4] Guerrero JM, Vasquez JC, Matas J, de Vicuna LG, Castilla M. Hierarchical control of droop-controlled AC and DC microgrids—A general approach toward standardization. IEEE Trans Ind Electron 2011;58(1):158–72.
[5] Fachini F, Bogodorova T, Vanfretti L, Boersma S. A microgrid control scheme for islanded operation and re-synchronization utilizing model predictive control. Sustain Energy, Grids Networks 2024;39:101464.
[6] Bidram A, Nasirian V, Davoudi A, Lewis FL. Cooperative synchronization in distributed microgrid control. In: Advances in industrial control, Cham, Switzerland: Springer International Publishing; 2017.
[7] Li Q, Yan C, Han Y, Zeng H, Zalhaf AS, Yang P, Wang C. Optimizing power sharing and voltage control in DC microgrids using a novel adaptive droop control strategy based on current consensus algorithm. Sustain Energy, Grids Networks 2024;38:101386.
[8] Guo L, Liu X, Li X, Wang R, Ren H, Wang Z, Sun Q. A novel adaptive droop-based SoC balancing control strategy for distributed energy storage system in DC microgrid. Int J Electr Power Energy Syst 2025;165:110514.
[9] Sun Y, Zhong C, Hou X, Yang J, Han H, Guerrero JM. Distributed cooperative synchronization strategy for multi-bus microgrids. Int J Electr Power Energy Syst 2017;86:18–28.
[10] Shah S, Sun H, Nikovski D, Zhang J. Consensus-based synchronization of microgrids at multiple points of interconnection. In: 2018 IEEE power & energy society general meeting. Portland, OR: IEEE; 2018, p. 1–5.
[11] Li Z, Zhang J, Cheng Z, Si J, Wang Y, Wang X. Distributed cooperative grid synchronization strategy for multiple parallel grid-supporting inverters in AC microgrid. Int J Electr Power Energy Syst 2024;155:109624.
[12] Tomás-Martín A, García-Cerrada A, Sigrist L, Yagüe S, Miguel DR, Martín-Utrilla F-D. Re-synchronisation of a microgrid to the main grid using multi-agent secondary control. In: 2023 IEEE belgrade powerTech. Belgrade, Serbia: IEEE; 2023, p. 1–6.
[13] Khan MYA, Liu H, Shang J, Wang J. Distributed hierarchal control strategy for multi-bus AC microgrid to achieve seamless synchronization. Electr Power Syst Res 2023;214:108910.
[14] Olfati-Saber R, Murray R. Consensus problems in networks of agents with switching topology and time-delays. IEEE Trans Autom Control 2004;49(9):1520–33.
[15] Wong YCC, Lim CS, Cruden A, Rotaru MD, Ray PK. A consensus-based adaptive virtual output impedance control scheme for reactive power sharing in radial microgrids. IEEE Trans Ind Appl 2021;57(1):784–94.
[16] Coelho EAA, Wu D, Guerrero JM, Vasquez JC, Dragicevic T, Stefanovic C, Popovski P. Small-signal analysis of the microgrid secondary control considering a communication time delay. IEEE Trans Ind Electron 2016;63(10):6257–69.
[17] Chen Y, Wan K, Zhao J, Yu M. Accurate consensus-based distributed secondary control with tolerance of communication delays for DC microgrids. Int J Electr Power Energy Syst 2024;155:109636.
[18] Liu C, Wang X, Zhang H. Adaptive event-triggered H∞ consensus secondary control for islanded microgrids under multiple time delays. Electr Power Syst Res 2024;232:110367.
[19] Shahab MA, Mozafari B, Soleymani S, Dehkordi NM, Shourkaei HM, Guerrero JM. Stochastic consensus-based control of uGs with communication delays and noises. IEEE Trans Power Syst 2019;34(5):3573–81.
[20] Dehkordi NM, Khorsandi A, Baghaee HR, Sadati N, Moghaddam SS, Guerrero JM. Voltage and frequency consensusability of autonomous microgrids over fading channels. IEEE Trans Energy Convers 2021;36(1):149–58.
[21] MATLAB. version 9.7.0 (R2019b). Natick, Massachusetts: The MathWorks Inc.; 2019.
[22] Yazdani A, Iravani R. Grid-imposed frequency VSC system: Control in dq-frame. In: Voltage-sourced converters in power systems: modeling, control, and applications. John Wiley and Sons, Ltd; 2010, p. 160–203.
[23] Bidram A, Davoudi A, Lewis FL. A multiobjective distributed control framework for islanded AC microgrids. IEEE Trans Ind Informatics 2014;10(3):1785–98.
[24] Meng L, Dragicevic T, Roldán-Pérez J, Vasquez JC, Guerrero JM. Modeling and sensitivity study of consensus algorithm-based distributed hierarchical control for DC microgrids. IEEE Trans Smart Grid 2016;7(3):1504–15.
[25] Diestel R. Graph theory. New York: Springer; 2000, p. 415,
[26] Sun Y, Hou X, Yang J, Han H, Su M, Guerrero JM. New perspectives on droop control in AC microgrid. IEEE Trans Ind Electron 2017;64(7):5741–5.
[27] Jankovic N, Roldán-Pérez J, Prodanovic M, Rouco L. Centralised multimode power oscillation damping controller for photovoltaic plants with communication delay compensation. IEEE Trans Energy Convers 2024;39(1):311–21.
[28] Wang X, Li YW, Blaabjerg F, Loh PC. Virtual-impedance-based control for voltage-source and current-source converters. IEEE Trans Power Electron 2015;30(12):7019–37.
[29] Pagola FL. Control systems. Madrid, Spain: Universidad Pontificia Comillas; 2016.
[30] Tomás-Martín A, García-Cerrada A, Sigrist L, Yagüe S, Suárez-Porras J. State relevance and modal analysis in electrical microgrids with high penetration of electronic generation. Int J Electr Power Energy Syst 2023;147:108876.
[31] Rodríguez-Cabero A, Roldán-Pérez J, Prodanovic M. Virtual impedance design considerations for virtual synchronous machines in weak grids. IEEE J Emerg Sel Top Power Electron 2020;8(2):1477–89.
[32] Roldán-Pérez J, Bueno EJ, Peña-Alzola R, Rodríguez-Cabero A. All-pass-filter-based active damping for VSCs with *LCL* filters connected to weak grids. IEEE Trans Power Electron 2018;33(11):9890–901.
[33] Pogaku N, Prodanovic M, Green TC. Modeling, analysis and testing of autonomous operation of an inverter-based microgrid. IEEE Trans Power Electron 2007;22(2):613–25.
[34] Tomás-Martín A, Zuluaga-Ríos CD, Suárez-Porras J, Kazemtabrizi B, García-Aguilar J, Sigrist L, García-Cerrada A. A vector-based flexible-complexity tool for simulation and small-signal analysis of hybrid AC/DC power systems. Sustain Energy, Grids Networks 2025;43:101817.
[35] VFlexP. 2025, https://github.com/atomasmartin/VFlexP, GitHub repository.
[36] Du W, Lasseter RH, Khalsa AS. Survivability of autonomous microgrid during overload events. IEEE Trans Smart Grid 2019;10(4):3515–24.